# A Computational Framework for Parachute Inflation Based on Immersed Boundary/Finite Element Approach

*HUANG Yunyao*[1], *ZHANG Yang*[1,2*], *PU Tianmei*[3], *JIA He*[2,4], *WU Shiqing*[2,4], *ZHOU Chunhua*[5]

1. College of Astronautics, Nanjing University of Aeronautics and Astronautics, Nanjing 211106, P.R. China;
2. Laboratory of Aerospace Entry, Descent and Landing Technology, CASC, Beijing 100094, P.R. China;
3. College of Electrical, Energy and Power Engineering, Yangzhou University, Yangzhou 225127, P.R. China;
4. Beijing Institute of Space Mechanics and Electricity, Beijing 100096, P.R. China;
5. College of Aeronautics, Nanjing University of Aeronautics and Astronautics, Nanjing 210016, P.R. China

(Received 23 January 2024; revised 16 August 2024; accepted 18 August 2024)

**Abstract:** A computational framework for parachute inflation is developed based on the immersed boundary/finite element approach within the open-source IBAMR library. The fluid motion is solved by Peskin's diffuse-interface immersed boundary (IB) method, which is attractive for simulating moving-boundary flows with large deformations. The adaptive mesh refinement technique is employed to reduce the computational cost while retain the desired resolution. The dynamic response of the parachute is solved with the finite element approach. The canopy and cables of the parachute system are modeled with the hyperelastic material. A tether force is introduced to impose rigidity constraints for the parachute system. The accuracy and reliability of the present framework is validated by simulating inflation of a constrained square plate. Application of the present framework on several canonical cases further demonstrates its versatility for simulation of parachute inflation.

**Key words:** parachute inflation; fluid-structure interaction; immersed boundary method; finite element method; adaptive mesh refinement

**CLC number:** V411 **Document code:** A **Article ID:** 1005-1120(2024)04-0502-13

## 0 Introduction

Parachute inflation involves the complex fluid-structure interaction (FSI) phenomena which is highly nonlinear and unsteady, therefore making it quite challenging to simulate.

The last few decades have seen tremendous development of numerical methods for solving the FSI problem of parachute inflation. One of the most popular methods is the deforming-spatial-domain/stabilized space-time (DSD/SST) method[1-2], by which the detailed description of the flow field and structural response during the parachute inflation process can be obtained. This method has been continuously developed by involving new version and special techniques to address the computational challenges, such as the geometric complexities of the parachute canopy and the contact between parachutes in a cluster[3-7]. As a commercially available transient dynamic finite element code, LS-DYNA has been well adapted to FSI simulation of parachute inflation in a number of real-world applications[8-12]. The immersed boundary (IB) method[13] is an attractive numerical method for FSI simulation of parachute inflation because it does not require dynamic generation of body-fitted meshes, making it suitable for tackling problems involving large structural deformations or displacements. Kim and Peskin[14-15] used the IB method to study the semi-opened parachute

*Corresponding author, E-mail address: zhy@nuaa.edu.cn.

**How to cite this article**: HUANG Yunyao, ZHANG Yang, PU Tianmei, et al. A computational framework for parachute inflation based on immersed boundary/finite element approach[J]. Transactions of Nanjing University of Aeronautics and Astronautics, 2024, 41(4): 502-514.

http://dx.doi.org/10.16356/j.1005-1120.2024.04.007

in both two and three dimensions. Liu et al.[16] proposed an IB-lattice Boltzmann (LB) based FSI solver to study the inflation process of several types of parachute systems.

IBAMR is a distributed-memory parallel implementation of the IB method with support for adaptive mesh refinement (AMR) of the Cartesian grid[17]. Core IBAMR functionality relies upon several high-quality open-source libraries[17], including: SAMRAI[18], PETSc[19], libMesh[20], and hypre[21]. IBAMR has been widely used in simulations of various FSI problems involving large deformations[22-26].

In this work, a computational framework for parachute inflation is developed based on the immersed boundary/finite element approach within the open-source IBAMR library. The fluid motion is solved by the diffuse-interface IB method prposed by Peskin[13]. Adaptive mesh refinement is employed to reduce the computational cost while retaining the desired resolution. The dynamic response of the parachute is solved with the finite element approach. The flow field and structural response are analyzed to demonstrate the capability of the developed framework for solving parachute inflation problems. The framework could be further extended to study the inflation process of various parachute systems for different aerospace missions. Simulation of parachute inflation is mainly based on the conventional body-fitted methods, e.g., the arbitary Lagrangian-Eulerian (ALE) method and the DSD/SST method. Application of the IB method for parachute inflation is still rare. When dealing with large deformation objects, the body-fitted methods may suffer from severe mesh distortion, while this issue can be avoided by using the IB method. To our knowledge, this is the first endeavor to implement the computational framework for parachute inflation within the IBAMR library. The remainder of this paper is organized as follows. In Section 1, the numerical methods are introduced. In Section 2, the inflation of the constrained square plate is simulated to validate the accuracy and reliability of the present FSI framework. In Section 3, applications of the present FSI framework for simulating parachute inflation are presented and discussed. Section 4 summarizes the study and shows some prospects to the future work.

# 1 Numerical Methods

## 1.1 Governing equations

In the present study, the parachute system immersed in a viscous incompressible fluid is modeled. Let $\Omega=\Omega_f\cup\Omega_s$ denote the computational domain occupied by the fluid-structure system, where $\Omega_f$ and $\Omega_s$ are respectively the fluid and structure domain, $x$ denotes the Eulerian Cartesian coordinates, and $\chi(X,t)$ represents the physical position of Lagrangian point $X$ at time $t$. The governing equations which can be used for solving parachute inflation are[27-28]

$$\rho\frac{\mathrm{D}\boldsymbol{u}}{\mathrm{D}t}(\boldsymbol{x},t)=-\nabla p(\boldsymbol{x},t)+\mu\nabla^2\boldsymbol{u}(\boldsymbol{x},t)+\boldsymbol{f}(\boldsymbol{x},t) \tag{1}$$

$$\nabla\cdot u(x,t)=0 \tag{2}$$

$$f(\boldsymbol{x},t)=\int_{\Omega_s}\nabla_X\cdot\boldsymbol{P}_s(\boldsymbol{X},t)\,\delta\big(\boldsymbol{x}-\chi(\boldsymbol{X},t)\big)\,\mathrm{d}X-\int_{\partial\Omega_s}\boldsymbol{P}_s(\boldsymbol{X},t)\,\boldsymbol{N}(\boldsymbol{X})\,\delta\big(\boldsymbol{x}-\chi(\boldsymbol{X},t)\big)\,\mathrm{d}A(\boldsymbol{X}) \tag{3}$$

$$\frac{\partial\chi}{\partial t}(\boldsymbol{X},t)=\int_{\Omega}\mathrm{m}u(\boldsymbol{x},t)\,\delta\big(\boldsymbol{x}-\chi(\boldsymbol{X},t)\big)\,\mathrm{d}\boldsymbol{x} \tag{4}$$

where $\rho$ is the mass density, $\frac{\mathrm{D}\boldsymbol{u}}{\mathrm{D}t}(\boldsymbol{x},t)$ the material derivative, $p(\boldsymbol{x},t)$ the pressure, $\boldsymbol{u}(\boldsymbol{x},t)$ the Eulerian velocity field, $\boldsymbol{f}(\boldsymbol{x},t)$ the Eulerian elastic force density, $\mu$ the dynamic viscosity of the fluid, $\delta(\boldsymbol{x})$ the Dirac delta function, $\boldsymbol{N}(\boldsymbol{X})$ the outward unit normal along the structure boundary, $\mathrm{d}A$ the area differentials, and $\boldsymbol{P}_s(\boldsymbol{X},t)$ the first Piola-Kirchhoff stress tensor which is used for describing the structure response. $\boldsymbol{P}_s(\boldsymbol{X},t)$ can be derived from the strain energy function depending on the constitutive law of the material, and the expression will be given in the following subsection.

A two-dimensional (2D) schematic of the Eulerian-Lagrangian grid layout is illustrated in Fig.1 to introduce the discretization of the governing equations. In the Eulerian framework, the mesh spacing is denoted as $(\Delta x_1,\Delta x_2)$. For a given cell $(i,j)$, the pressure is approximated at the cell center as $p_{i,j}$,

whereas the velocity components are approximated at the center of cell edges, i.e., $x_{i-\frac{1}{2},j}=\left(i\Delta x_1,\left(j+\frac{1}{2}\right)\Delta x_2\right)$ and $x_{i,j-\frac{1}{2}}=\left(\left(i+\frac{1}{2}\right)\Delta x_1,j\Delta x_2\right)$ as $(u_1)_{i-\frac{1}{2},j}$ and $(u_2)_{i,j-\frac{1}{2}}$, respectively. A second-order staggered-grid finite difference method is used to discretize the incompressible Navier-Stokes equations. In the Lagrangian framework, as shown in Fig.1, the structure is superimposed on the background Eulerian mesh and represented by discretized marker points at positions $\{X_l\}_{l=1}^m$, where $m$ is the number of marker points. A nodal finite element (FE) method is employed to discretize the structure equations with the FE basis functions denoted as $\{\phi_l(X)\}_{l=1}^m$. The Eulerian-Lagrangian interaction is achieved by passing information between the two frameworks through the Dirac delta function in Eq.(3). For more details, Refs.[27, 29] can be referred.

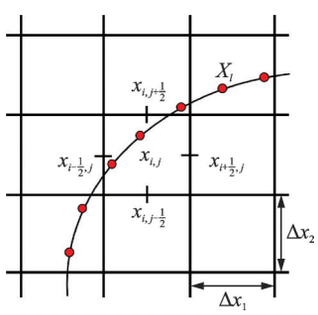


Fig.1 Schematic of the Eulerian-Lagrangian grid layout

## 1.2 Material models

In the present study, the fabrics of the canopy and cable are modeled with the hyperelastic nonlinear material, specifically the Neo-Hookean model and Saint Venant-Kirchhoff model[30]. Note that the material for the cable is assumed with uniaxial extension, therefore only the axial stress of the cable is considered and other stress components are negligible by comparison.

### 1.2.1 Neo-Hookean model

By introducing volumetric stabilization to the structural stress, the modified strain energy function for the Neo-Hookean model can be split into the deviatoric and dilatational part[29]

$$\Psi=\frac{G}{2}\left(J^{-2/3}I_1-3\right)+\frac{\kappa_{\text{stab}}}{2}(\ln J)^2 \tag{5}$$

where $J$ is the Jacobian determinant of the deformation gradient $\boldsymbol{F}$; $I_1$ the first invariant of the right Cauchy-Green deformation tensor, i.e., $I_1=\lambda_1^2+\lambda_2^2+\lambda_3^2$ and $\lambda_i$ are the principal stretches; $G$ the shear modulus which can be calculated as $G=\frac{E}{2(1+\nu)}$ with $E$ the Young's modulus and $\nu$ the Poisson's ratio; $\kappa_{\text{stab}}$ the numerical bulk modulus which can be related to $G$ via $\kappa_{\text{stab}}=\frac{2G(1+\nu_{\text{stab}})}{3(1-2\nu_{\text{stab}})}$ with $\nu_{\text{stab}}$ the numerical Poisson's ratio.

The corresponding first Piola-Kirchhoff stress tensor can then be expressed as[29]

$$\boldsymbol{P}_{\text{s}}=GJ^{-2/3}\left(\boldsymbol{F}-\frac{I_1}{3}\boldsymbol{F}^{-\text{T}}\right)+\kappa_{\text{stab}}\ln J\boldsymbol{F}^{-\text{T}} \tag{6}$$

### 1.2.2 Saint Venant-Kirchhoff model

The strain energy function for the Saint Venant-Kirchhoff model can be expressed as

$$\Psi=\frac{\lambda}{2}\left(\text{tr}(\boldsymbol{E})\right)^2+\mu\,\text{tr}(\boldsymbol{E}^2) \tag{7}$$

where $\boldsymbol{E}$ is the Green-Lagrange strain tensor with the expression of

$$\boldsymbol{E}=\frac{1}{2}(\boldsymbol{C}-\boldsymbol{I}) \tag{8}$$

where $\boldsymbol{C}=\boldsymbol{F}^{\text{T}}\boldsymbol{F}$ is the right Cauchy-Green deformation tensor and $\boldsymbol{I}$ the identity tensor. The coefficients $\mu$ and $\lambda$ are the Lamé constants, which are related to the material properties through the Young's modulus $E$ and the Poisson's ratio $\nu$.

$$\mu=\frac{E}{2(1+\nu)},\ \lambda=\frac{E\nu}{(1+\nu)(1-2\nu)} \tag{9}$$

The corresponding first Piola-Kirchhoff stress tensor can then be expressed as

$$\boldsymbol{P}_{\text{s}}=\boldsymbol{F}\left(\lambda\,\text{tr}(\boldsymbol{E})\boldsymbol{I}+2\mu\boldsymbol{E}\right) \tag{10}$$

## 1.3 Tether forces

Note that the intersection point where the parachute cables meet should be fixed, therefore a tether force needs to be imposed on that point. The tether force is approximated by a Lagrange multiplier $\boldsymbol{F}(\boldsymbol{X},t)$[27], shown as

$$\boldsymbol{F}(\boldsymbol{X},t)=\kappa\left(\chi(\boldsymbol{X},0)-\chi(\boldsymbol{X},t)\right)-\eta\frac{\partial\chi}{\partial t}(\boldsymbol{X},t) \tag{11}$$

where $\kappa$ is a stiffness penalty parameter and $\eta$ a damping penalty parameter for reducing numerical oscillations from moderate to high Reynolds numbers. Note that the values of $\kappa$ and $\eta$ are case-dependent and determined with the trial-and-error method.

### 1.4 Numerical implementation

The developed framework for FSI simulation of the parachute inflation is established within the IBAMR library. Specifically, the IBFE module in IBAMR based on the IB-finite element (FE) method[27] is employed, where adaptive mesh refinement of the background Cartesian mesh relies on SAMRAI[18], FE analysis of the parachute system relies on libMesh[20], and the IB and FE solver rely on the PETSc library[19].

## 2 Validation

The canopy is the main component of the parachute system that undergoes large deformations during inflation. Therefore, inflation of a constrained square plate is chosen as a benchmark case to model the canopy-solely situation such that the accuracy and reliability of the present FSI solver can be validated.

Following the computational setup in Ref. [16], a square elastic plate is placed in a uniform flow $U_\infty = 1$ m/s, and the length and thickness of the plate are $L = 0.812\,8$ m and $h = 5 \times 10^{-3}$ m, respectively. The inflation model of the plate is shown in Fig.2. Note that the corners of the plate are constrained by the tether forces, and the plate is discretized with 2 704 hexahedral elements. The Neo-Hookean hyperelastic material model is applied to the plate with a shear modulus of $G = 3.85 \times 10^2$ Pa, equivalent to a Young's modulus $E = 1 \times 10^3$ Pa. In addition, the Saint Venant-Kirchhoff hyperelastic model with the same Young's modulus and Poisson's ratio is also used for comparison.

The computational domain is shown in Fig.3. The size of the domain is 8 m × 4 m × 4 m in the $x$, $y$ and $z$ directions. The left side of the domain is the inlet with a Dirichlet velocity boundary condition, and the right side of the domain is the outlet with a Neumann velocity boundary condition. The other four sides of the domain are specified with the free-slip-wall boundary condition. The computational domain is discretized with an adaptively refined Cartesian mesh with three nested mesh levels (highlighted in red, green and blue in Fig.3) and the refinement ratio between adjacent levels is 4. In Fig.3, the subscripts 1, 2 and 3 correspond to the $x$, $y$ and $z$ directions, respectively. The number of cells on the coarsest mesh level is $N = 16$. The mesh interval on the finest level is $\Delta x = 1.5 \times 10^{-2}$ m and the computational time step is $\Delta t = 1 \times 10^{-4}$ s. The mesh factor ratio between the finest Eulerian mesh and Lagrangian mesh is $M_{\mathrm{FAC}} = 1.0$. The drag coefficient of the plate $C_{\mathrm{D}}$ is defined as

$$C_{\mathrm{D}} = \frac{F_{\mathrm{D}}}{\frac{1}{2}\rho U_\infty^2 A} \tag{12}$$

where $F_{\mathrm{D}}$ and $A$ are the drag force and nominal area of the plate, respectively. Note that the drag coeffi-

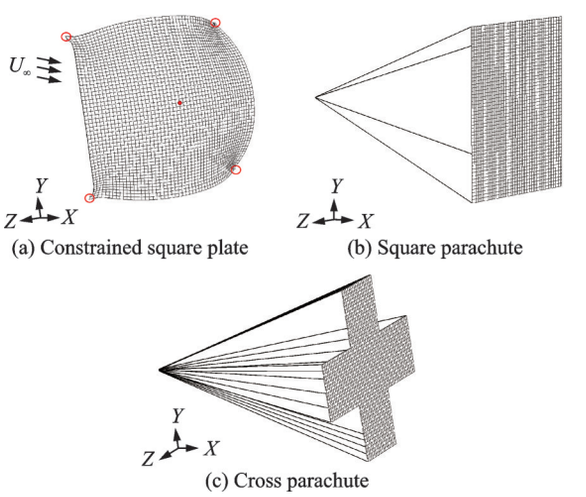


Fig.2 Inflation models

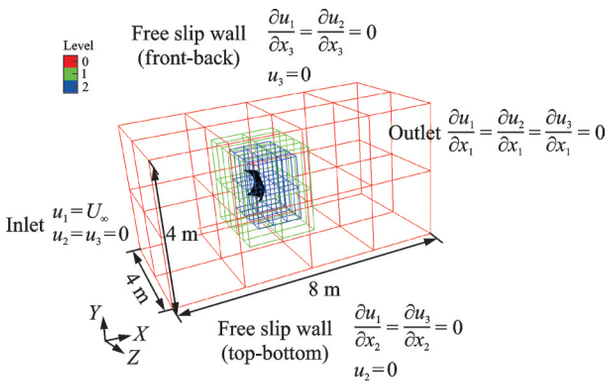


Fig.3 Computational domain of the constrained square plate

cient for the subsequent parachute cases can also be calculated by Eq.(12).

Time history of the drag coefficient for the plate with different material properties is plotted in Fig.4(a). The peak value of $C_D$ obtained by the Saint Venant-Kirchhoff model is much higher than that obtained by the Neo-Hookean model, whereas the stable value of $C_D$ for the Saint Venant-Kirchhoff model is a bit lower than that obtained by the Neo-Hookean model. The stable values of $C_D$ for both models are around 1.2. Time traces of $C_D$ obtained by an IB-LB FSI solver[16] with the same computational setup are superimposed on this figure for comparison. Note that in their computation, different values of Young's modulus of the plate are tested. The peak values of $C_D$ obtained by the present solver is larger than those obtained by the IB-LB FSI solver, and this could be attributed to the different material models used in the literature. For the same value of $E=1\times10^3$ Pa, comparison of the stable value of $C_D$ is listed in Table 1. From Table 1, it can be seen that the relative error between the

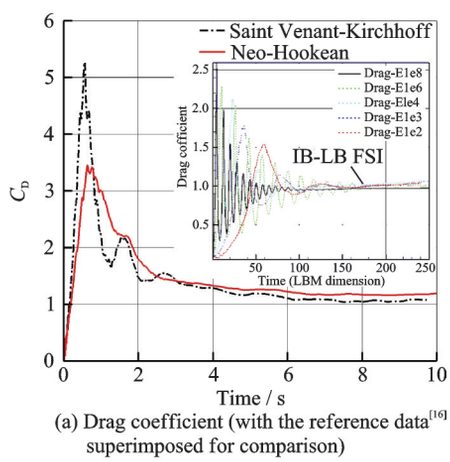


(a) Drag coefficient (with the reference data[16] superimposed for comparison)

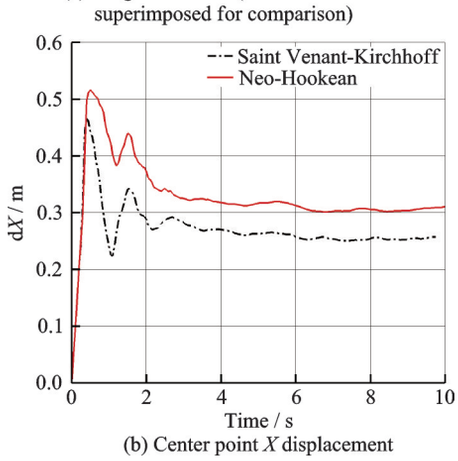


(b) Center point $X$ displacement

Fig.4 Time history results of the constrained square plate

**Table 1 Comparison of the stable value of $C_D$ for the constrained square plate with $E=1\times10^3$ Pa**

| Parameter | Liu et al.[16] | Present | Relative error |
|---|---|---|---|
| $C_D$ | 1.1 | 1.18 | 7.3% |

stable values of $C_D$ obtained by the IB-LB FSI solver and the present solver is around 7%, thus validating the accuracy and reliability of the present FSI solver.

Time history of the displacement for the center point of the plate (red dot in Fig.2(a)) in the $x$ direction is illustrated in Fig.4(b). Note that the results for different material models are also compared. The peak and stable displacements for the Neo-Hookean model are approximately 0.52 m and 0.3 m, while those for the Saint Venant-Kirchhoff model are around 0.46 m and 0.26 m. The Neo-Hookean material can bear larger deformation than the Saint Venant-Kirchhoff material for this canopy-solely case. Moreover, the deformed shapes of the plate at different time instants are shown in Fig.5, where the pseudocolor indicates the magnitude of displacement in the $x$ direction. Bulges at the four corners gradually become larger and expand to the plate center to reach a steady shape of the plate. Similar phenomenon can be observed in Ref.[16].

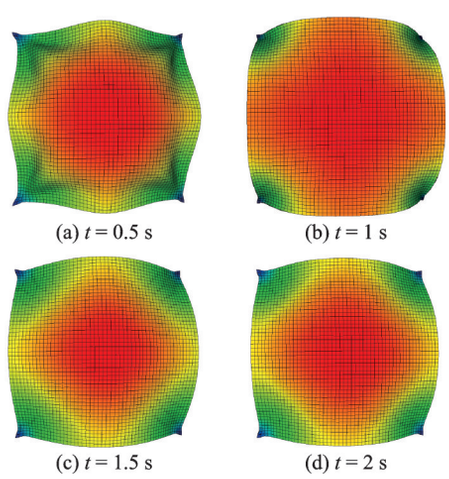

(a) $t=0.5$ s (b) $t=1$ s

(c) $t=1.5$ s (d) $t=2$ s

Fig.5 Deformation of the constrained square plate

## 3 Application

In this section, the present FSI solver is applied for simulation of parachute inflation under several scenarios.

Note that due to the challenge of IB methods for simulating turbulent flows[31], the Reynolds number is reduced to $Re=\frac{\rho U_\infty L}{\mu_f}=1\times10^4$ without involving any turbulence model for all the cases in the numerical experiments, where $\rho$ is the mass density, $U_\infty$ the incoming flow velocity, $L$ the length of the canopy, and $\mu_f$ the dynamic viscosity of the air. Since the inflated canopy can be treated as a bluff body, the dominant source of drag comes from the pressure drag, therefore this treatment is acceptable.

It should also be mentioned that the full inflation process of the parachute starts from the folded form. However, this work is focused on simulating from the flat unfolded state which is also important for understanding the parachute inflation process[7,15-16].

### 3.1 Inflation of a square canopy parachute

In this subsection, the inflation process of a square parachute in a uniform flow is simulated. Fig.2(b) shows the inflation model of the square parachute. The four cables are connected to a fixed point by the tether forces and tied to the corners of the canopy surface to move together with the canopy. Following the case setup in Ref.[16], the length of the cable is $l=1.27$ m, and the fixed point is placed at the origin of the coordinate system. The cross section of the cable is approximated as a circle with the radius $r=1\times10^{-3}$ m. The Neo-Hookean and Saint Venant-Kirchhoff material models are applied. The Young's modulus of the cable is $E=1\times10^7$ Pa, and the Poisson's ratio is zero to allow for uniaxial extensions of the cable. For the canopy, we keep the Poisson's ratio the same as that for the square plate case, while the Young's modulus is $E=1\times10^4$ Pa which corresponds to a stiffer material. The geometry parameters of the canopy, size of the computational domain, boundary conditions, mesh interval on the finest mesh level, and the mesh factor ratio $M_{FAC}$ are kept the same as those for the square plate case.

Time history of the drag coefficient and center point displacement of the canopy in the $x$ direction for the square parachute with different material models is plotted in Figs.6(a) and (b), respectively. From these figures, it can be observed that for this stiffer material, the discrepancies between the Neo-Hookean and Saint Venant-Kirchhoff models are relatively small. The stable value of $C_D$ is approximately 1.1. Compared with the stable value of $C_D$ reported in Ref.[16], the relative error between them is within 10%. The peak and stable displacements of the center point are approximately 0.5 m and 0.3 m, respectively, which are also very close to the values reported in Ref.[16]. The deformation of the square parachute obtained by the Neo-Hookean model at different time instants is shown in Fig.7, where the pseudocolor indicates the magnitude of displacement in the $x$ direction. Due to the effect of dynamically changing fluid and elastic forces, the breathing phenomenon of the parachute can be observed from this figure. The deformation of the parachute is significant within the first one second, and after that the shape of the parachute does not change much.

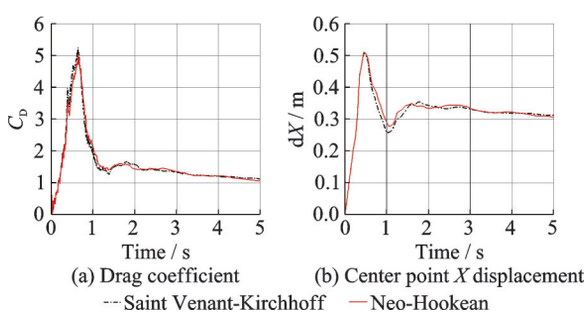


Fig.6 Time history results of the square parachute

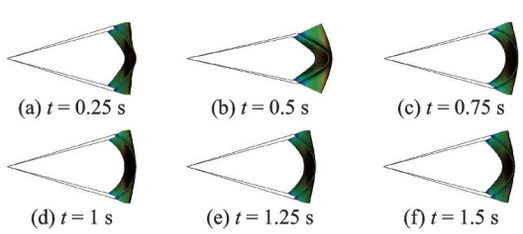


Fig.7 Deformation of the square parachute

Fig.8 shows the instantaneous vortex iso-surface $Q=40$ of the plate for the Neo-Hookean model. Note that for each time instant, the corresponding adaptively refined mesh with three nested mesh levels is also illustrated. From Fig.8, it can be observed that dynamic evolution of the vortex shedding behind the plate can be accurately captured by

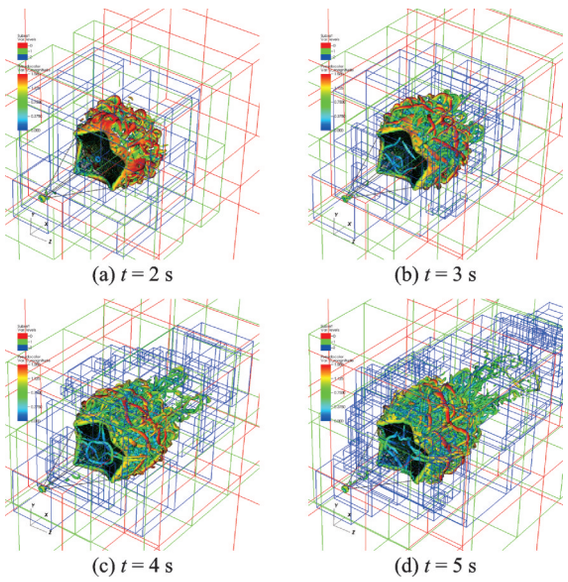


Fig.8 Instantaneous vortex iso-surface $Q=40$ of the square parachute

the adaptively refined mesh.

### 3.2 Inflation of a cross canopy parachute

In this subsection, the inflation process of a cross parachute with twenty elastic cables is simulated. Fig.2(c) shows the inflation model of the cross parachute. The twenty cables are connected to a fixed point by the tether forces and tied to the outer edges of the canopy surface to move together with the canopy. Following the case setup in Ref.[16], the distance from the fixed point to the initial canopy surface is equal to that for the square parachute case. The computational setup and material properties of the canopy and cables are also the same as those for the square parachute.

Time history of the drag coefficient for the cross parachute with different material models is plotted in Fig.9(a). For this case with softer material, the peak value of $C_D$ obtained by the Saint Venant-Kirchhoff model is higher than that obtained by the Neo-Hookean model, whereas the stable value for both models are almost the same. Note that for both material models, two peaks can be observed during the inflation process which correspond to the significant breathing phenomenon. The stable value of the drag coefficient is $C_D=0.8$, which falls into the typical range (0.6—0.85) of the drag coefficient for a cross parachute[32].

In addition, time history of the displacement for the center point of the canopy in the $x$ direction with different material models is illustrated in Fig.9(b). From this figure, we can see that the time instants where the two peaks happen are consistent with those in Fig.9(a) for both models. The deformation of the cross parachute obtained by the Neo-Hookean model at different time instants is shown in Fig.10, where the pseudocolor indicates the magnitude of displacement in the $x$ direction. The breathing phenomenon of the cross canopy can be observed from this figure.

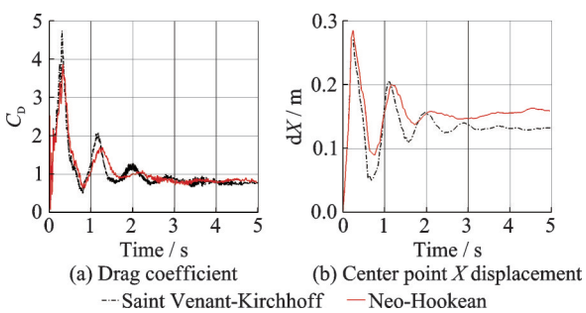


Fig.9 Time history results of the cross parachute

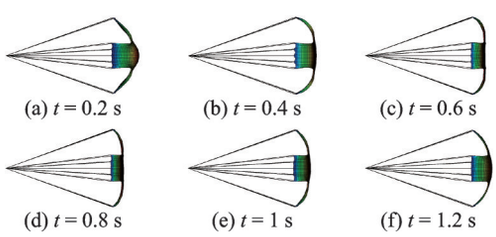


Fig.10 Deformation of the cross parachute

### 3.3 Inflation of double cross canopy parachutes

In this subsection, the inflation process of double cross canopy parachutes is studied to demonstrate the capability of the present framework for multiple parachutes simulation.

Fig.11 shows the deployment of the double cross parachutes. The geometric model of each cross parachute is identical to the one used for the single cross parachute case. The layout of the double cross parachutes is obtained by rotating the initial model (see Fig.2(c)) about the $z$ axis with an angle of $2\pi/15$ and $-2\pi/15$, respectively, and therefore a gap can exist between the two canopies to avoid any possible overlap or contact. The cables

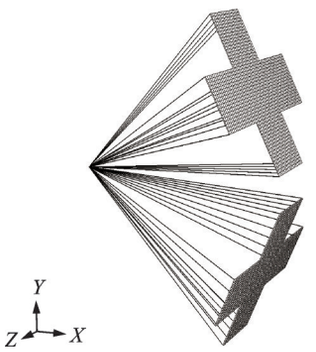


Fig.11 Deployment of double cross parachutes

are connected to a fixed point by the tether forces and tied to the outer edges of the canopy surface to move together with the canopy. The computational setup and material properties of the canopy and cables are the same as the single parachute case. For this case, only the Neo-Hookean material model is used.

Comparison of the drag coefficient for the single and double cross parachutes is plotted in Fig.12. The time instants corresponding to peak values of $C_D$ for both parachutes are almost the same, whereas the whole inflation process of double cross parachutes is more stable than the single cross parachute due to the larger canopy area. The stable value of drag coefficient for double cross parachutes is $C_D = 1.0$, which is approximately 1.25 times the drag coefficient for the single parachute.

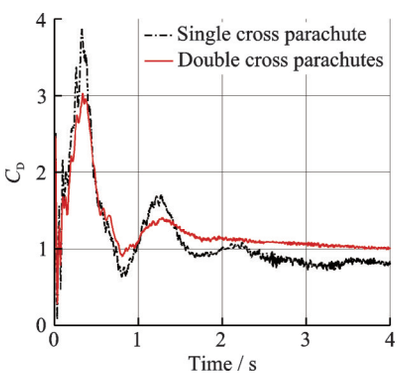


Fig.12 Comparison of the drag coefficient for single and double cross parachutes

The deformation of the double cross parachutes at different time instants are shown in Fig.13. Compared with the deformation of single cross parachute in Fig.10, it takes less time for the double cross

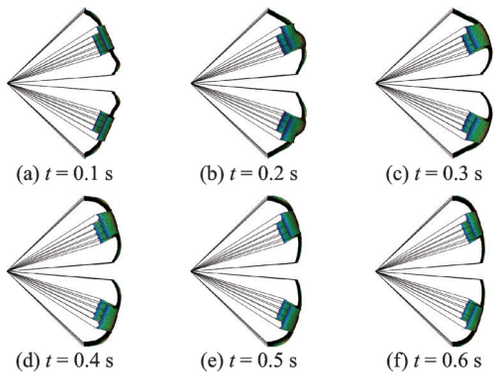


Fig.13 Deformation of double cross parachutes

parachutes to reach a stable inflated shape.

Fig.14 depicts the slice view of the velocity field around the canopies at different time instants. At the beginning stage of the inflation process, the wake flow behind the canopies is symmetrical and a jet flow is formed through the gap between canopies. The jet flow is then mixed with the shedding vortex behind the canopies, and the flow structure is gradually evolved to turbulent flow.

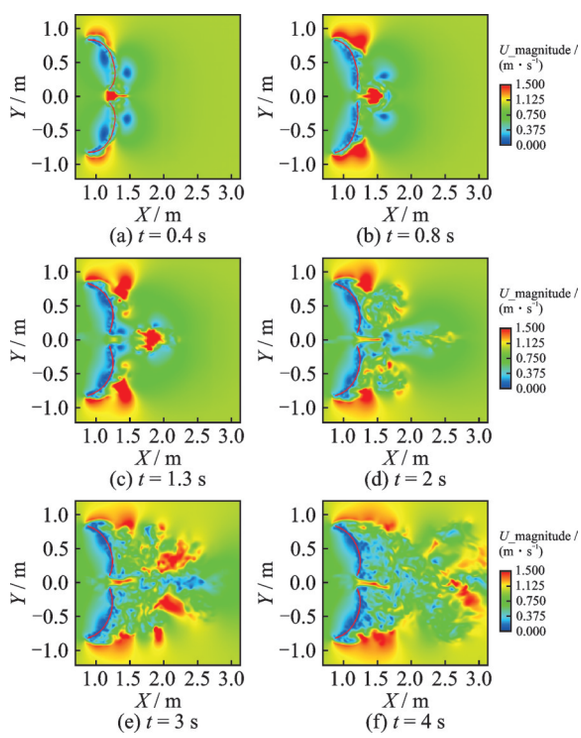


Fig.14 Near-canopy velocity field of double cross parachutes

We need to point out that further simulation for inflation of parachute clusters can be readily implemented in the present framework with minimal efforts.

### 3.4 Deployment of windows on cross parachute canopy

In this subsection, the effect of window deployment on the inflation of the cross parachute is investigated.

As shown Fig.15, three types of window deployment are chosen: (1) One window on the center of the canopy; (2) one window on the center of one arm; (3) two windows on adjacent arms with each on the center of the arm. The window is square with an area $L^2/81$, where $L$ is the canopy length. For different window deployments, the computational setup is the same as the baseline case in Subsection 3.2, and the Neo-Hookean material model is considered.

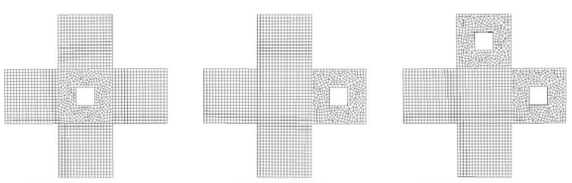


Fig.15 Deployment of windows on cross parachute canopy

Comparison of the drag coefficient for different window deployments on the canopy is shown in Fig.16. From this figure, we can draw several conclusions: (1) Window deployment can generally improve the air permeability of the canopy; (2) for one window deployment, the position of the window has little effect on $C_D$; (3) increasing number of windows can significantly reduce the maximum value of $C_D$, but cannot significantly reduce the stable value of $C_D$; (4) for one-window deployment, $C_D$ can be approximately reduced by 18%, while for two-window deployment, $C_D$ can be further reduced by approximately 3%. In general, these findings are consistent with those observed from a ringsail-type parachute with windows deployment[33].

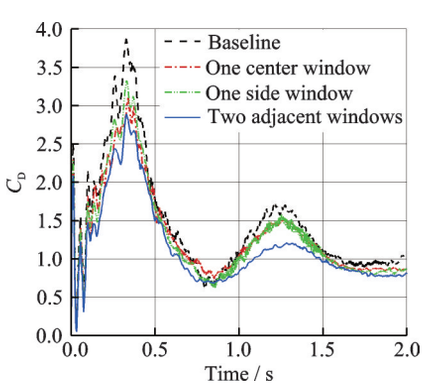


Fig.16 Comparison of drag coefficient for different deployments of windows on cross parachute canopy

Furthermore, Fig.17 shows the instantaneous near-canopy velocity field for different window deployments. Note that for cases with one-window deployment, the slice is cut through the $xy$ plane, while for the case with two-window deployment, the slice is cut through the $xz$ plane to view the flow through the second window. The jet flow is formed through the window at different locations and mixed with the shedding vortex. The phenomenon of canopy curling along the edge of the window can also be observed.

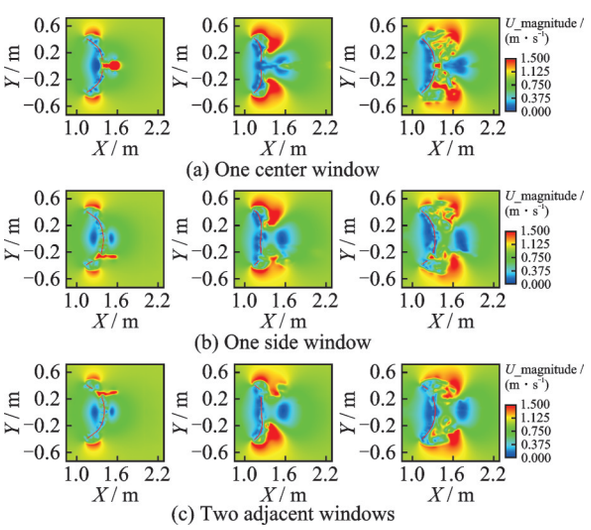


Fig.17 Near-canopy velocity field for different window deployments of cross parachute

### 3.5 Active tension on cross canopy parachute

In this subsection, we propose a solution to modulate the parachute deformation and the surrounding flow field within the present framework, which could be used for the design of the low-cost steerable parachutes[11,34].

An active tension prescribed by a time-dependent stress is used on cables of the cross parachute to play the role of muscle actuators. Similar to the elastic stress $\boldsymbol{P}_s$, this active stress can be expressed in the form of the first Piola-Kirchoff stress tensor as[35]

$$\boldsymbol{P}_{\mathrm{a}}=JT\boldsymbol{F}\boldsymbol{f}_0\boldsymbol{f}_0^{\mathrm{T}} \tag{13}$$

where $J$ is the Jacobian determinant of the deformation gradient $\boldsymbol{F}$, $T$ the magnitude of prescribed active tension, and $\boldsymbol{f}_0$ the direction vector of the prescribed tension with respect to the reference configuration.

The total stress calculated on the parachute then becomes

$$\boldsymbol{P}=\boldsymbol{P}_{\mathrm{s}}+\boldsymbol{P}_{\mathrm{a}} \tag{14}$$

The initial setup of this case is the same as that in Subsection 3.2, and the Neo-Hookean material model is employed. After the inflation process of the cross parachute reaches a stable state at $t=2$ s (see Fig.9), an active tension with the magnitude $T=1\times10^3$ N in the direction $\boldsymbol{f}_0=(-1,0,0)$ is used on five cables connecting with the same canopy arm. A schematic for applying active tension on the cross parachute is depicted in Fig.18.

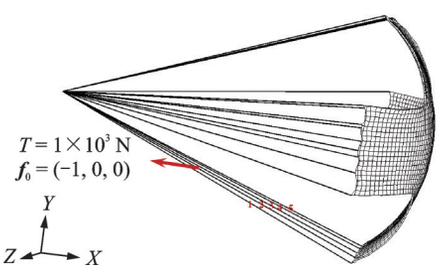


Fig.18 Schematic for applying active tension on cross parachute cables

Comparison of the drag coefficient for the cross parachute with and without active tension is plotted in Fig.19. After applying the active tension, significant change and oscillation of the drag coefficient can be observed especially between $t=2.0$—$2.2$ s. After that, the oscillation becomes small and the parachute is gradually deformed to a new stable state.

Time evolution of the near-canopy flow field with and without active tension is compared in Fig.20. We select four time instants where the discrepancy of $C_{\mathrm{D}}$ between them is large. At $t=2.04$ s, large velocity magnitude can be observed near the canopy end where the tension is applied, and the initial stable state of the parachute

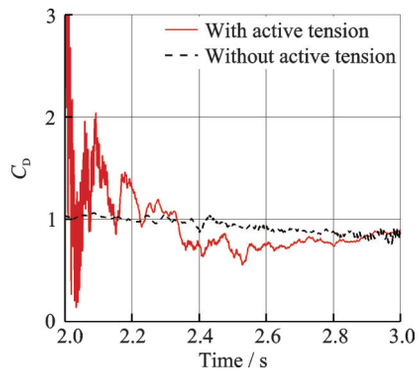


Fig.19 Comparison of drag coefficient for cross parachute with and without active tension

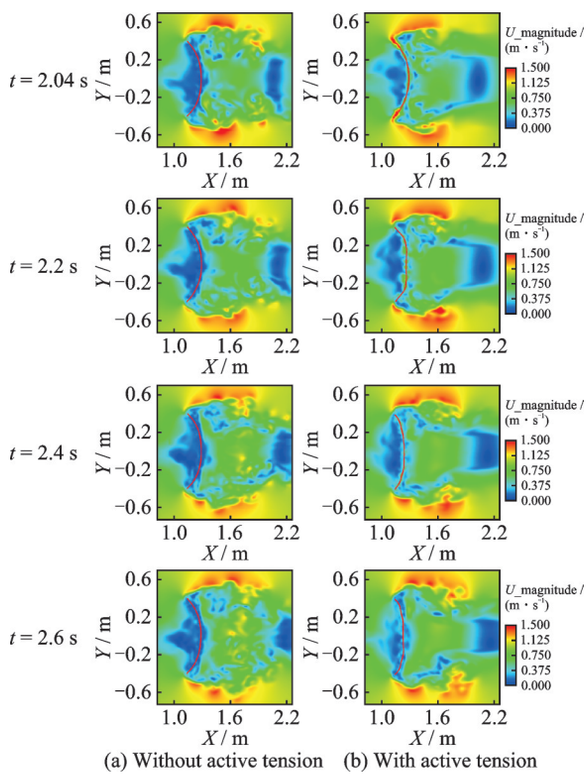


Fig.20 Comparison of the near-canopy velocity field for cross parachute with and without active tension

with fully inflated canopy and stretched cables is disrupted. At $t=2.2$ s, 2.4 s, 2.6 s, with active tension used, the canopy shape becomes irregular with small grooves, which affects the surrounding flow field.

## 4 Conclusions

This work explores the feasibility of implementing a reliable computational framework for FSI simulation of parachute inflation under the open-source environment. Specifically, the IBFE module

in the open-source IBAMR library based on the immersed boundary/finite element approach is employed, and adaptive mesh refinement of the background Cartesian mesh is also supported. The canopy and cables of the parachute system are modeled with the Neo-Hookean and Saint Venant-Kirchhoff hyperelastic materials, and tether forces are introduced to impose rigidity constraints.

Inflation of a benchmark constrained square plate is simulated to validate the accuracy and reliability of the present framework. Investigations on several application cases such as multiple parachute systems, window deployment on the canopy, and steerable parachutes by using active tensions further demonstrate the versatility of the present framework for simulation of parachute inflation.

Compared to the widely used ALE method[7] which may suffer from mesh distortion and interpolation errors due to mesh movement for parachute inflation, the present method offers advantages in terms of simplified mesh handling, flexibility with complex geometries, ease of implementation, stability and computational efficiency. These advantages make it particularly suitable for FSI simulation of parachute inflation, which involves large deformations, complex interfaces, and high computational demands. In addition, the AMR technique is employed in the present method, which could save considerable computational time while retain the mesh resolution and accuracy.

Nevertheless, there are several limitations for the present study: (1) All the cases are directly conducted under $Re = 1 \times 10^4$ without involving any turbulence model, whereas the Reynolds number for a real parachute is typically around $10^5$ to $10^6$[15] which requires high resolution of the turbulent boundary layer; (2) air permeability for the canopy fabric is not considered. Therefore, future work will be focused on addressing the above limitations to extend the framework for simulating parachute inflation in real aerospace applications, e. g., ringsail parachute clusters for heavy loads, and parafoils for precision airdrop.

**References**

[1] TEZDUYAR T E, BEHR M, LIOU J. A new strategy for finite element computations involving moving boundaries and interfaces—The deforming-spatial-domain/space-time procedure: I. The concept and the preliminary numerical tests[J]. Computer Methods in Applied Mechanics and Engineering, 1992, 94(3): 339-351.

[2] TEZDUYAR T E, BEHR M, MITTAL S, et al. A new strategy for finite element computations involving moving boundaries and interfaces—The deforming-spatial-domain/space-time procedure: Ⅱ. Computation of free-surface flows, two-liquid flows, and flows with drifting cylinders[J]. Computer Methods in Applied Mechanics and Engineering, 1992, 94(3): 353-371.

[3] TEZDUYAR T E, SATHE S, KEEDY R, et al. Space-time finite element techniques for computation of fluid-structure interactions[J]. Computer Methods in Applied Mechanics and Engineering, 2006, 195(17/18): 2002-2027.

[4] TEZDUYAR T E, SATHE S. Modelling of fluid-structure interactions with the space-time finite elements: Solution techniques[J]. International Journal for Numerical Methods in Fluids, 2007, 54(6/7/8): 855-900.

[5] TEZDUYAR T E, SATHE S, SCHWAAB M, et al. Fluid-structure interaction modeling of ringsail parachutes[J]. Computational Mechanics, 2008, 43(1): 133-142.

[6] TEZDUYAR T E, TAKIZAWA K, MOORMAN C, et al. Space-time finite element computation of complex fluid-structure interactions[J]. International Journal for Numerical Methods in Fluids, 2010, 64(10/11/12): 1201-1218.

[7] STEIN K, BENNEY R, KALRO V, et al. Parachute fluid-structure interactions: 3-D computation[J]. Computer Methods in Applied Mechanics and Engineering, 2000, 190(3/4): 373-386.

[8] TUTT B, TAYLOR A. The use of LS-DYNA to simulate the inflation of a parachute canopy[C]//Proceedings of 2005 18th AIAA Aerodynamic Decelerator Systems Technology Conference and Seminar. [S. l.]: AIAA, 2005: 1608.

[9] TUTT B A. Fluid structure interaction parachute benchmark models in LS-DYNA[C]//Proceedings of 2013 AIAA Aerodynamic Decelerator Systems (ADS) Conference. [S.l.]: AIAA, 2013: 1384.

[10] YANG L, WANG L, YU L, et al. Fluid-structure interaction study on the influence of circular gap of parachute on inflation performance with fixed payload[J]. Journal of Engineered Fibers and Fabrics, 2015, 10(1): 155892501501000119.

[11] FAGLEY C P, SEIDEL J, MCLAUGHLIN T E, et al. Computational study of air drop control mechanisms for cruciform parachutes[C]//Proceedings of 2017 24th AIAA Aerodynamic Decelerator Systems Technology Conference. [S.l.]: AIAA, 2017: 3541.

[12] NOETSCHER G, ROSE T M, BERGERON K. Modeling and experimental efforts towards robust low-cost cruciform canopy control[C]//Proceedings of 2019 AIAA Aviation 2019 Forum. [S.l.]: AIAA, 2019: 3371.

[13] PESKIN C S. The immersed boundary method[J]. Acta Numerica, 2002, 11: 479-517.

[14] KIM Y, PESKIN C S. 2-D parachute simulation by the immersed boundary method[J]. SIAM Journal on Scientific Computing, 2006, 28(6): 2294-2312.

[15] KIM Y, PESKIN C S. 3-D parachute simulation by the immersed boundary method[J]. Computers & Fluids, 2009, 38(6): 1080-1090.

[16] LIU F, LIU G, SHU C. Fluid-structure interaction simulation based on immersed boundary-lattice Boltzmann flux solver and absolute nodal coordinate formula[J]. Physics of Fluids, 2020, 32(4): 047109.

[17] GRIFFITH B E. IBAMR: An adaptive and distributed-memory parallel implementation of the immersed boundary (IB) method[EB/OL]. (2016-06-17)[2022-02-12]. https://ibamr.github.io/.

[18] HORNUNG R D, KOHN S R. Managing application complexity in the samrai object-oriented framework[J]. Concurrency and Computation: Practice and Experience, 2002, 14(5): 347-368.

[19] BALAY S, GROPP W, MCINNES L C, et al. Petsc, the portable, extensible toolkit for scientific computation[C]//Proceedings of 1998 Argonne National Laboratory. [S.l.]: [s.n.],1998: 2.

[20] KIRK B S, PETERSON J W, STOGNER R H, et al. libMesh: A C++ library for parallel adaptive mesh refinement/coarsening simulations[J]. Engineering with Computers, 2006, 22(3): 237-254.

[21] FALGOUT R D, YANG U M. hypre: A library of high performance preconditioners[C]//Proceedings of 2002 International Conference on Computational Science. [S.l.]: [s.n.], 2002: 632-641.

[22] BHALLA A P S, BALE R, GRIFFITH B E, et al. A unified mathematical framework and an adaptive numerical method for fluid-structure interaction with rigid, deforming, and elastic bodies[J]. Journal of Computational Physics, 2013, 250: 446-476.

[23] FENG L, GAO H, GRIFFITH B, et al. Analysis of a coupled fluid-structure interaction model of the left atrium and mitral valve[J]. International Journal for Numerical Methods in Biomedical Engineering, 2019, 35(11): 3254.

[24] GRIFFITH B E, PATANKAR N A. Immersed methods for fluid-structure interaction[J]. Annual Review of Fluid Mechanics, 2020, 52: 421.

[25] LEE J H, RYGG A D, KOLAHDOUZ E M, et al. Fluid-structure interaction models of bioprosthetic heart valve dynamics in an experimental pulse duplicator[J]. Annals of Biomedical Engineering, 2020, 48(5): 1475-1490.

[26] CAI L, ZHANG R, LI Y, et al. The comparison of different constitutive laws and fiber architectures for the aortic valve on fluid-structure interaction simulation[J]. Frontiers in Physiology, 2021, 725(12): 682893.

[27] GRIFFITH B E, LUO X. Hybrid finite difference/finite element immersed boundary method[J]. International Journal for Numerical Methods in Biomedical Engineering, 2017, 33(12): 2888.

[28] BOFFI D, GASTALDI L, HELTAI L, et al. On the hyper-elastic formulation of the immersed boundary method[J]. Computer Methods in Applied Mechanics and Engineering, 2008, 197(25/26/27/28): 2210-2231.

[29] VADALA-ROTH B, ACHARYA S, PATANKAR N A, et al. Stabilization approaches for the hyperelastic immersed boundary method for problems of large-deformation incompressible elasticity[J]. Computer Methods in Applied Mechanics and Engineering, 2020, 365: 112978.

[30] GAO H, MA X, QI N, et al. A finite strain nonlinear human mitral valve model with fluid-structure interaction[J]. International Journal for Numerical Methods in Biomedical Engineering, 2014, 30(12): 1597-1613.

[31] IACCARINO G, VERZICCO R. Immersed boundary technique for turbulent flow simulations[J]. Applied Mechanics Reviews, 2003, 56(3): 331-347.

[32] BEHR V. Development of the weapon borne sensor parachute system[C]//Proceedings of 1998 15th

Aerodynamic Decelerator Systems Technology Conference. [S.l.]: [s.n.], 1998: 1740.

[33] BAO W, JIA H, XUE X. Influence of "windows" structure on inflation process of ringsail parachute[J]. Acta Aeronautica et Astronautica Sinica, 2023, 44(5): 176-186.

[34] FIELDS T D, YAKIMENKO O A. Development of a steerable single-actuator cruciform parachute[J]. Journal of Aircraft, 2018, 55(3): 1041-1049.

[35] HOOVER A P, PORRAS A J, MILLER L A. Pump or coast: The role of resonance and passive energy recapture in medusan swimming performance[J]. Journal of Fluid Mechanics, 2019, 863: 1031-1061.

**Acknowledgement** This work was supported by the Open Project of Key Laboratory of Aerospace EDLA, CASC (No.EDL19092208).

**Authors** Mr. **HUANG Yunyao** received the M.S. degree in aerospace engineering from Nanjing University of Aeronautics and Astronautics, Nanjing, China, in 2024. His research interest is numerical simulation of parachute deceleration.

Dr. **ZHANG Yang** received the Ph.D. degree from Nanjing University of Aeronautics and Astronautics, Nanjing, China, in 2016. He is currently an associate professor with the Nanjing University of Aeronautics and Astronautics. His current research interest includes fluid-structure interaction.

**Author contributions** Mr. **HUANG Yunyao** completed the calculations, conducted analysis, and wrote and revised the manuscript. Dr. **ZHANG Yang** designed the study, reviewed and revised the original draft, and contributed to funding acquisition. Dr. **PU Tianmei** reviewed and revised the manuscript. Mr. **JIA He** reviewed and revised the manuscript. Mr. **WU Shiqing** reviewed and revised the manuscript. Prof. **ZHOU Chunhua** reviewed and revised the manuscript. All authors commented on the manuscript draft and approved the submission.

**Competing interests** The authors declare no competing interests.

(Production Editor: WANG Jing)

# 一种基于浸没边界/有限元方法的降落伞充气计算框架

黄云尧[1]，张　扬[1,2]，濮天梅[3]，贾　贺[2,4]，武士轻[2,4]，周春华[5]

(1.南京航空航天大学航天学院，南京 211106，中国；
2.航天科技集团航天进入减速与着陆技术实验室，北京 100094，中国；
3.扬州大学电气与能源动力工程学院，扬州 225127，中国；
4.北京空间机电研究所，北京 100096，中国；
5.南京航空航天大学航空学院，南京 210016，中国)

**摘要**：基于开源IBAMR库中的浸没边界/有限元方法，开发了一个用于模拟降落伞充气的计算框架。流体运动采用Peskin的扩散界面浸没边界(Immersed boundary, IB)方法进行求解，该方法适用于模拟涉及大变形的动边界流动。采用自适应网格细化技术，以降低计算成本，同时保持所需的网格分辨率。降落伞的动态响应通过有限元方法求解，降落伞系统的伞衣和伞绳采用超弹性材料建模。通过引入牵引力对降落伞系统施加刚性约束。利用受约束的方板充气过程验证了该框架的准确性和可靠性。该框架在多个典型算例中的应用进一步展示了其在降落伞充气模拟中的多功能性。

**关键词**：降落伞充气；流固耦合；浸没边界方法；有限元方法；网格自适应